Differential electron yield imaging with STXM

William A. Hubbard[1,2], Jared J. Lodico[1,2], Xin Yi Ling[1,2], Brian Zutter[1,2], Young-Sang Yu[3], David Shapiro[3], B. C. Regan[1,2]

[1] *Department of Physics and Astronomy, University of California, Los Angeles, CA 90095, U.S.A.*

[2] *California NanoSystems Institute, University of California, Los Angeles, CA 90095, U.S.A.*

[3] *Advanced Light Source, Lawrence Berkeley National Laboratory, Berkeley, CA, 94720, U.S.A.*

Abstract

Total electron yield (TEY) imaging is an established scanning transmission X-ray microscopy (STXM) technique that gives varying contrast based on a sample's geometry, elemental composition, and electrical conductivity. However, the TEY-STXM signal is determined solely by the electrons that the beam ejects from the sample. A related technique, X-ray beam-induced current (XBIC) imaging, is sensitive to electrons and holes independently, but requires electric fields in the sample. Here we report that multi-electrode devices can be wired to produce differential electron yield (DEY) contrast, which is also independently sensitive to electrons and holes, but does not require an electric field. Depending on whether the region illuminated by the focused STXM beam is better connected to one electrode or another, the DEY-STXM contrast changes sign. DEY-STXM images thus provide a vivid map of a device's connectivity landscape, which can be key to understanding device function and failure. To demonstrate an application in the area of failure analysis, we image a 100 nm, lithographically-defined aluminum nanowire that has failed after being stressed with a large current density.

Keywords: `STXM, TEY, XBIC, scanning transmission X-ray microscopy, electron yield, failure analysis`

1. Introduction

In scanning transmission X-ray microscopy (STXM), a focused X-ray beam is rastered across a thin sample, and the measured transmission is associated with the beam position to form an image. With soft (100–2,200 eV) X-rays, STXM offers distinct advantages over other spectromicroscopy techniques. Its sub-50 nm[1, 2, 3] spatial resolution is better than the $\sim 1\,\mu$m resolution of Raman imaging, and its beam-induced radiation damage is less that that of electron energy loss spectroscopy (EELS) in a transmission electron microscope (TEM) [4, 5]. STXM has found broad application in the biological [3, 6, 7] and physical [8, 9, 10] sciences, and has been used to study device physics in solar cells [11, 12], spin-torque memory[13], resistive memory[14] , and the Li-ion battery cathode material Li_xFePO_4[15].

STXM characterizes physical structure: it determines a sample's morphology and can even spectroscopically quantify a sample's chemical composition. However, in some cases the information returned is still too crude to identify gross characteristics of the sample that are of paramount importance. For instance, in an electronic device two conductors might be separated by a few nanometers of insulator. Conventional STXM might identify copper on one side and aluminum on the other, but, with its limited spatial resolution, conventional STXM is ill-suited to determine whether the two conductors are electrically connected. Because of the intimate relation between connectivity and function in electronic devices, determining the presence (or absence) and properties of such a connection might be the primary motivation for imaging the sample in the first place.

A conventional STXM system detects the transmitted X-rays with, for example, a photodiode on the beam-exit side of the sample. To expand its ca-

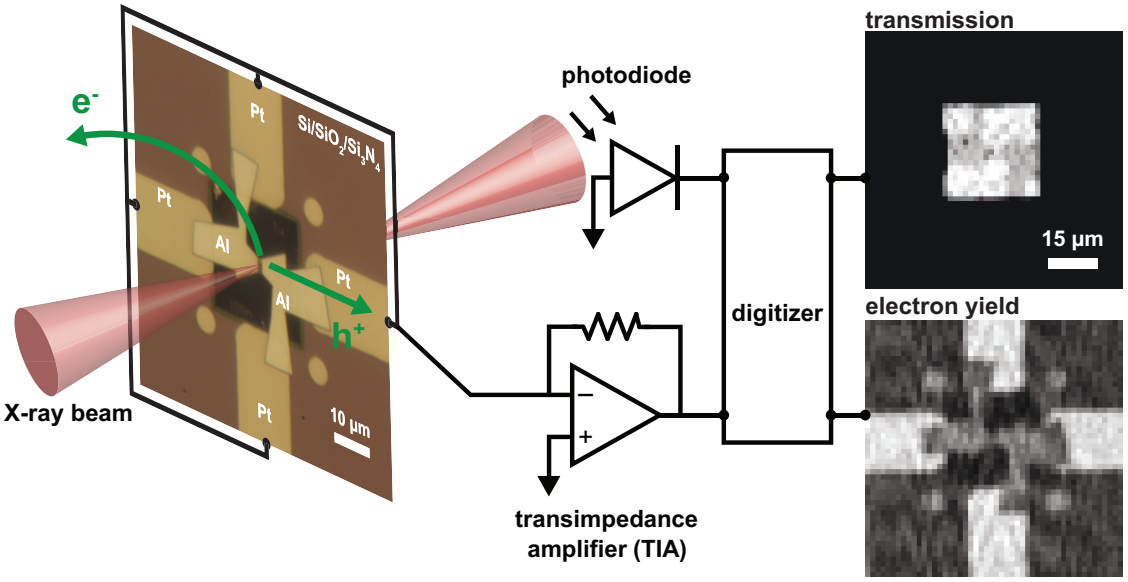

Figure 1: **Experiment overview.** The sample (optical image on left) consists of a 200 μm-thick silicon chip supporting a 20 nm-thick silicon nitride membrane. Platinum leads over the silicon contact an aluminum pattern that tapers to an unresolved wire in the membrane's center. Here all of the Pt leads are shorted together to produce a TEY image. As the X-ray beam (red) scans the sample, the signal from the photodiode and the transimpedance amplifier (i.e. TIA, or current meter) are digitized simultaneously to form the images on the right. The photodiode signal generates the standard STXM image (top right). The TIA measures the current produced in the sample by the X-ray beam (bottom right). When the beam ejects electrons from the sample, the resulting hole current is positive and is displayed with bright contrast.

pabilities, STXM imaging techniques that instead rely on electron detection have been developed. Among the most prominent are total electron yield (TEY) and X-ray beam-induced current (XBIC) imaging. TEY is performed either by capturing electrons emitted from the sample in a remote electron detector [16, 1], or by measuring the resulting holes with a current meter attached to the sample [17, 1]. TEY measures beam-ejected electrons of all energies, including primary[1], secondary, and Auger electrons[18]. XBIC, on the other hand, requires a current meter attached to the sample. It measures the current generated when the X-ray beam produces electron-hole pairs that are subsequently separated by local electric fields inside the sample [11, 12, 19, 20]. Generally XBIC signals, where present, are larger than TEY signals, because more electron-hole pairs than ejected electrons are produced per primary X-ray.

[1]In the X-ray microscopy community a primary electron is one scattered in a collision with beam X-ray, while in the electron microscopy community a primary electron is a beam electron, and a secondary electron is one scattered by a primary. In this article we use the conventions of the X-ray community.

XBIC has an electron microscopy counterpart, (standard) electron beam-induced current (EBIC) imaging, where the electron-hole pairs are instead produced by a scanned electron beam [21, 22]. A related electron microscopy technique, secondary electron emission EBIC (SEEBIC) imaging [23, 24, 25], is closely analogous to TEY, and to the subject of this paper.

If the sample is wired for current collection, both TEY and XBIC imaging can be performed using the same apparatus, but with slightly different electrical connections. TEY requires only a single connection between the sample and the current meter (generally a transimpedance amplifier, or TIA)[19], while XBIC requires that the sample have an additional connection to a low impedance to allow for charge neutralization.

Using a sample wired with multiple electrical connections, as is characteristic of XBIC and not TEY, we perform STXM mapping of electron yield. However, the resulting contrast has its root in the ejection of electrons from the sample (and not in the creation of electron-hole pairs), as is characteristic of TEY and not XBIC. Here we report that using multiple electrodes allows differential electron yield

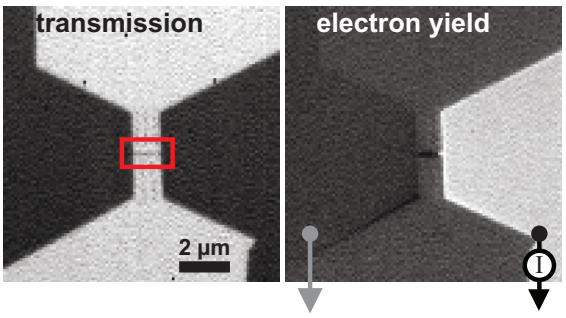

Figure 2: **STXM and DEY imaging of the Al nanowire device.** These images of the device of Fig. 1 are acquired with the left electrode grounded and the right electrode attached to the TIA (indicated schematically here with an "*I*" circumscribed by a circle). The field of view in these images corresponds to the x-ray transparent center of the Fig. 1 images, where the photodiode signal is bright. The standard STXM image (left) shows both Al leads with the same contrast, while the DEY image (right) indicates that only the Al lead on the right is electrically connected to the TIA. The red box indicates the region shown in Fig. 3.

(DEY) imaging, which gives contrast that changes sign between neighboring electrodes on the sample. For instance, when the X-ray beam is incident on an electrode connected to the current meter, the measured current is generally positive, since the ejected electrons leave a hole current behind. But when the beam moves to a neighboring, grounded electrode, the beam-induced hole current is shunted to ground and is therefore not measured. Meanwhile, some of the primary and secondary electrons ultimately return to the first electrode, where they are measured as a negative current (analogous to Fig. 2 of reference [23]). This negative current represents electrons that, in the absence of the current meter, would *not* have left the sample, thus by definition it is distinct from the TEY current. The resulting DEY contrast, unlike standard STXM, TEY, or XBIC contrast, can vividly reveal whether neighboring electrodes are connected.

Our implementation of DEY imaging employs a TEM sample holder, which has some particular advantages for *in situ* STXM imaging of electronic devices. The production of STXM-compatible, electrically connected samples shares many challenges with the production of samples for *in situ* TEM experiments. Accordingly, several X-ray beamlines have incorporated TEM stage/load-lock mechanisms in X-ray imaging systems, allowing for STXM experiments to be performed with TEM sample holders[26, 15, 27]. We adopt this approach [27], which gives access to the numerous off-the-shelf *in situ* capabilities afforded by specialized TEM holders, including imaging in liquid and gas, heating, cooling, biasing, and physical manipulation. The TEM stage and load-lock combination also makes for faster sample exchange (minutes instead of hours) and easier correlative TEM imaging (which can be performed without even removing the sample from the TEM sample holder).

2. Experimental

X-ray imaging is performed at Lawrence Berkeley National Lab's Advanced Light Source (ALS) on beamline 7.0.1.2 (COSMIC) [27]. The COSMIC beamline offers a 250–2500 eV X-ray energy range and a 50 nm spot size, and is equipped with a FEI CompuStage load-lock system, which accepts TEM sample holders. Except where indicated otherwise, STXM images are acquired with an incident beam energy of 1565 eV. To form STXM and electron yield images, the signals from a post-sample photodiode and a FEMTO DLPCA-200 TIA, respectively, are digitized simultaneously as the beam is rastered pixel-by-pixel across the sample. To acquire diffraction patterns for ptychography, the photodiode can be retracted to expose a CCD detector [28]. Data are reconstructed using standard methods available in the SHARP ptychography package [29]. Scanning TEM (STEM) imaging is performed in an FEI Titan 80–300 STEM at 80 kV. For both STXM and STEM the sample is mechanically supported and electrically contacted with a Hummingbird Scientific biasing TEM sample holder.

Our demonstration sample (Fig. 1 optical image) is a silicon chip patterned via optical lithography with four Ti/Pt (5/25 nm) electrodes that lead to a 20 nm-thick silicon nitride membrane[23]. On the membrane a 1-μm-long, 100-nm-wide, and 100-nm-thick Al wire is patterned via electron beam lithography. Tapered pads connect the wire to the Ti/Pt electrodes in a 4-wire configuration. Before being loaded in the STXM chamber, the wire is biased in vacuum until failure and then stored in the ambient atmosphere for several days. All images labeled "transmission" show the raw, unprocessed photodiode signal. All images labeled "electron yield" show the TIA signal, which has been Fourier filtered to remove AC line noise. TIA current values are given relative to the signal on the bare silicon nitride membrane, where very little electron yield is

expected. The optical density referenced in Figs. 5–6 is $-\ln \frac{I}{I_0}$, where I_0 is the photodiode signal on the bare silicon nitride membrane.

3. Results and Discussion

STXM imaging of the silicon nitride membrane window reveals the Al electrodes, which transmit fewer photons than the bare membrane and thus appear slightly darker (Fig. 1 top right). But STXM imaging of the silicon support frame provides no information, as the thick silicon blocks the incident X-rays. The (total) electron yield image, on the other hand, reveals device features in the entire field of view, even where the sample is opaque (Fig. 1 bottom right). The Al pads are visible, as in the STXM image, but so are the Pt electrodes to which the Al is connected. The Pt has a larger electron yield than the Al and therefore appears brighter. Four Pt islands at the corners of the membrane are also visible, despite the apparent lack of an electrical connection. Holes produced in these islands can evidently travel the several-micrometer distance to the Pt electrodes [23]. Contrast is slightly darker over the membrane, an insulator that generates few primary electrons in the beam.

Electron yield mapping can be extremely helpful in samples that are mostly opaque. With only the transmission-based contrast of standard STXM, locating a thin region is generally accomplished by trial-and-error, and is analogous to wandering around in the dark. Electron yield imaging turns the lights on: sample features far from the transparent area can be used as landmarks to locate the region of interest systematically and quickly.

The device of Fig. 1 features an unresolved Al wire that previously connected the two larger pads. Because the device has been subjected to a bias current sufficiently large to cause heating and eventual failure, the wire is broken and represents a very large electrical impedance. We image the nanowire of Fig. 1 again, this time with a smaller field of view (Fig. 2), but here we change the electrical connections for DEY imaging: the right Al electrode remains connected to the TIA but the left electrode is now grounded. (The biasing sample holder gives independent access to each of the four Ti/Pt electrodes, so this change can be made without breaking vacuum.)

In this configuration, when the X-ray beam ejects electrons from the right electrode, the TIA measures a positive (hole) current. When the X-ray beam ejects electrons from the left electrode, the hole current flows to ground directly and is not measured by the TIA. However, a fraction of the electrons emitted from the left electrode are recaptured[23] by the right electrode and are measured as a negative (electron) current. Thus, the resulting image (Fig. 2 right) shows each electrode as bright or dark respectively, depending on whether or not the electrode is directly connected to the TIA. Like TEY, DEY imaging maps whether or not a region is conducting: the Al on both sides of the break more readily emits primary electrons than the insulating Si_3N_4 support membrane. But DEY imaging also indicates the connectivity landscape, particularly the 'watershed' boundary of the region electrically connected to the TIA [23]. Such

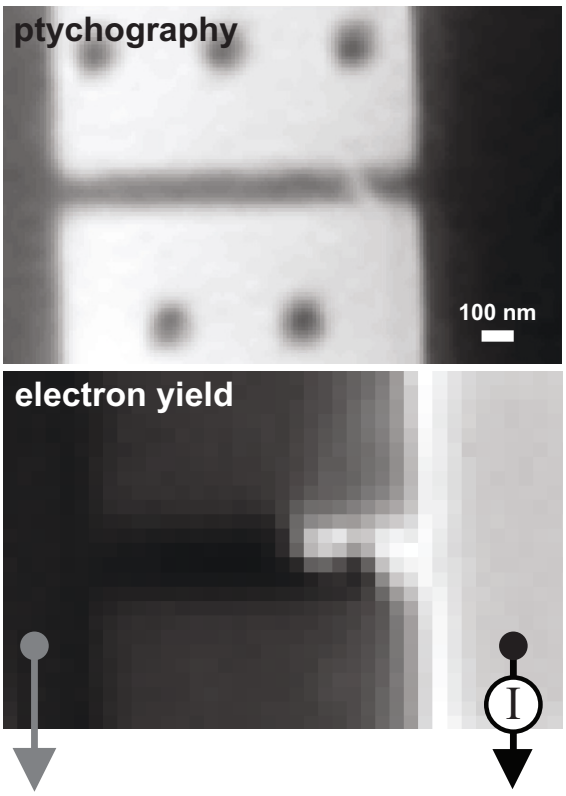

Figure 3: **Ptychography and DEY imaging of the Al nanowire device.** Retracting the photodiode and scanning over the region outlined in red in Fig. 2 produces, after reconstruction, a ptychography image (top) that reveals the break in the Al nanowire. The simultaneously acquired electron yield image (bottom) has the inferior resolution, relative to ptychography, of standard STXM, but it nonetheless reveals a surprising feature: electrical connectivity spans the 'break' in the Al wire that is seen in ptychographic image.

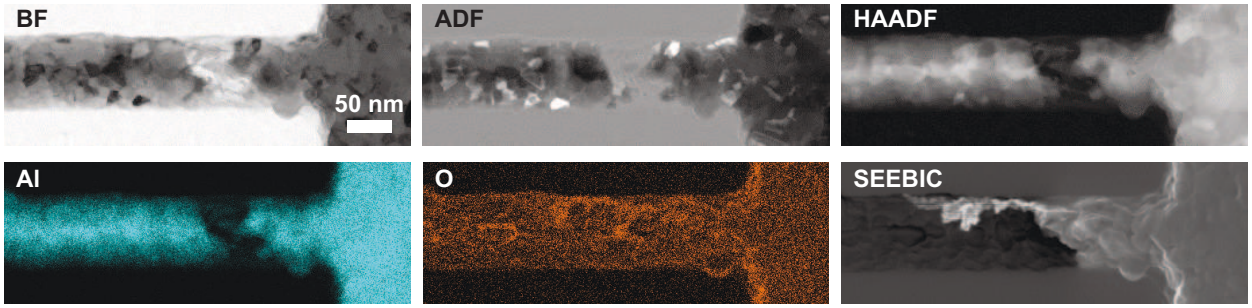

Figure 4: **STEM imaging of the Al nanowire device.** The Al wire of Figs. 1–3 is imaged with standard STEM (BF, ADF, and HAADF), STEM EDS elemental mapping (Al and O), and STEM SEEBIC. The BF and SEEBIC images are the electron microscopy analogues of the previously-shown STXM (Fig. 2) and DEY images (Figs. 2–3) respectively. The STEM images show similar contrast but significantly better spatial resolution relative to their analogous X-ray images.

differential contrast is not accessible with TEY.

Note that the dark contrast generated by electron recapture (e.g. the left electrode of Fig. 2 right) indicates that DEY imaging, on electrodes showing bright contrast (e.g. the right electrode of Fig. 2 right), always has a better signal-to-noise ratio than TEY imaging. The recaptured electron current has the opposite sign as the hole current. To the extent that these currents are equal and are collected by the same TIA, they cancel. Viewed from this perspective, TEY is a worst case scenario, in that the recapturing electrode spans the whole sample. It thus collects a correspondingly large recapture current, and generates a correspondingly small net current (i.e. signal). One can even imagine pathological geometries where a nearby, off-sample surface, such as an aperture [17], could produce enough primary and secondary electrons — which contain no information about the sample itself — to overwhelm the original hole current. Imaging a small electrode that alone is connected to the TIA gives the best case scenario, for here the recapture current is minimized and the measured hole current is undiminished.

Scans of the same device (Fig. 3) with even smaller fields of view (i.e. higher magnification) resolve both the physical and the electronic break in the Al wire. Here we retract the photodiode to capture the diffraction pattern generated at each X-ray beam position (i.e. pixel) for ptychography. Without the photodiode the standard STXM image is no longer available. Ptychographically reconstructing the captured diffraction patterns produces an image that reveals a break in the Al on the right side of the wire (Fig. 3 top). The break appears clean, with an ~ 50 nm length missing from the wire. The DEY image (Fig. 3 bottom), however, shows a more complicated structure around the break. The large Al lead on the right is bright, as expected based on the larger field of view (i.e. lower magnification) image of the same device (Fig. 2 right). But surprisingly, portions of the wire to the left of the 'break' (as identified by the ptychographic image) are also bright, indicating that they too are connected to the Al lead on the right.

During ptychographic imaging, the photodiode is retracted and thus its signal is not available. However, electron yield data can still be acquired simultaneously with the diffraction patterns used to produce the ptychographic image. And unlike the ptychographic data, the electron yield data is immediately viewable in a real-space format without any analysis (e.g. reconstruction or summing). The real-time feedback provided by electron yield imaging, like the ability to image opaque regions of a sample, is an experimental convenience that can save valuable time on the beamline.

The use of the TEM sample holder for X-ray imaging makes correlative microscopy especially straightforward. STEM (Fig. 4) imaging of the same device in the same sample holder confirms, with much improved spatial resolution, the device properties ascertained with X-ray imaging. Bright-field (BF), annular dark-field (ADF), and high-angle ADF (HAADF) STEM images (Fig. 4, top row) each show loss of material at the failure point, and energy-dispersive X-ray spectroscopy (EDS) elemental mapping (Fig. 4, bottom left and center) confirms that Al has disappeared in the gap. SEEBIC imaging (Fig. 4, bottom right) shows the same

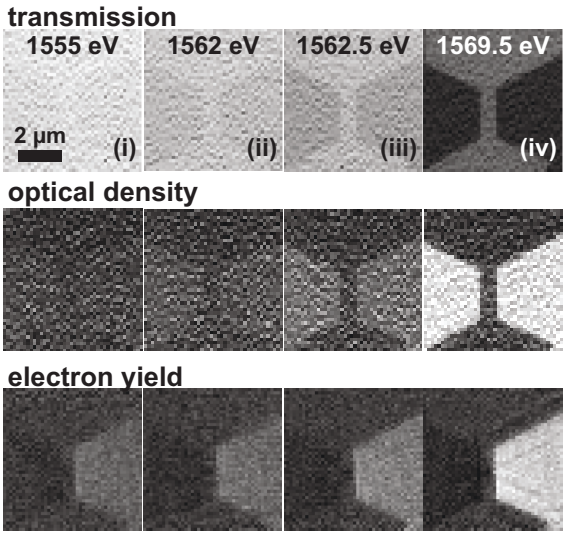

Figure 5: **STXM and electron yield images at four representative X-ray beam energies.** The beam energy for each column of representative images (see Fig. 6) is indicated. The electrodes are almost invisible in the raw photodiode (upper row) and calculated optical density (middle row) images below 1562 eV, while they are easily seen in the electron yield images (bottom row) over the entire energy range scanned (1555–1575 eV). The electron yield images are acquired with the circuit as indicated in Figs. 2–3. The contrast scale is held fixed for each row of images.

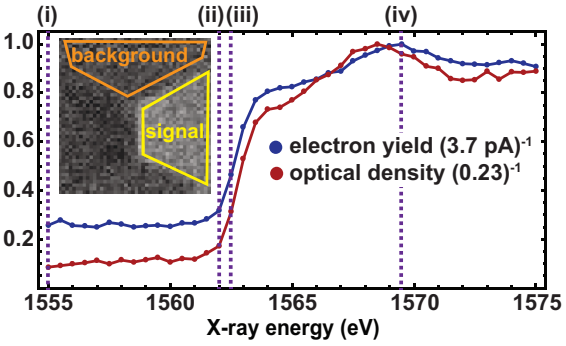

Figure 6: **Electron yield and optical density of an Al electrode as a function of incident beam energy.** Signal on the right electrode (inset, yellow) is plotted for the electron yield (blue curve) and optical density (red curve). Electron yield is measured relative to the background reference region (inset, orange). Both plots are normalized by dividing by the maximum value measured for each, which is indicated in the plot legend. Dashed lines indicate images shown in Fig. 5.

non-obvious electrical connectivity seen with DEY imaging, again with improved spatial resolution: the right electrode is electrically connected to material well to the left of the gap that appears in the standard imaging channels. Both the DEY and the SEEBIC [23] images are mapping the connectivity landscape as revealed by beam-induced ejection of electrons from the sample. Evidently the contrast is relatively insensitive to the type of probe beam (X-ray or electron) and is thus predominantly determined by the sample's conductivity distribution. While here electron microscopy has clearly superior spatial resolution, X-ray microscopy has spectroscopic advantages that will be discussed shortly.

Metallic aluminum in quantities below the detection limits here is likely responsible for this connectivity extension. Some correlation between the connectivity extension seen with DEY and SEEBIC imaging is seen in the oxygen EDS map, but nothing that would suggest the existence of the extension without the DEY (or SEEBIC) data. In many practical situations, DEY imaging's ability to detect the electrical connectivity created by dopants or other trace impurities in quantities below the standard detection methods' thresholds might be key to understanding device behavior.

In X-ray microscopy, unlike electron microscopy, the beam energy can be tuned across an absorption threshold of an element in the sample. (This capability has been exploited in previous XBIC work [20].) The differential contrast in the electron yield persists under such spectroscopic imaging. We scan the beam energy over 41 values encompassing the aluminum K-edge (1555 eV to 1575 eV in 0.5 eV steps). Below 1562 eV, the Al electrodes are difficult to detect in the STXM images, while they are obvious in the electron yield images (Fig. 5). Both signals become more intense (Fig. 6) as the energy exceeds the Al K-edge threshold at ∼1563 eV. The Al electron yield, which is already significant below the K-edge, increases by about 400% immediately above the K-edge.

Spectroscopic tuning of an X-ray beam may give DEY imaging an important advantage over SEEBIC imaging for the study of chemically heterogeneous samples. Figure 6 shows clear evidence of X-ray absorption fine structure (XAFS) in the DEY signal, as has been seen previously in the TEY signal [16, 1]. With the ability to spectroscopically to vary the electron yield according to elemental identity, molecular bonding, local disorder, and effective atomic charge, DEY imaging has the poten-

tial to directly relate the local chemistry to electrical transport properties, and thus give new insight into electrochemical systems ranging from batteries to doped semiconductors.

4. Conclusion

We have demonstrated STXM electron yield imaging of a simple device mounted in a TEM biasing holder. With a TEM load-lock installed, performing electron yield measurements requires no modification of the STXM chamber or the data acquisition electronics; all electrical connections to the device are made through the holder, and the electron yield signal is digitized in parallel with the existing photodiode signal. Measuring current from the entire device provides the standard TEY measurement, while grounding portions of the circuit gives DEY images that map connectivity within the device. In a broken Al nanowire, the differential contrast provided by DEY imaging precisely locates the failure point and reveals a non-obvious electrical connection spanning the physical gap in the wire. As a complement to standard STXM and ptychographic imaging, the DEY technique has a number of practical advantages, including real-time and opaque-region imaging. For functional studies of micro- and nano-scale electronic devices, DEY imaging makes a particularly powerful addition to the suite of available correlative imaging modes.

5. Acknowledgments

This work was supported by National Science Foundation (NSF) Science and Technology Center (STC) award DMR-1548924 (STROBE), by NSF awards DMR-1611036 and DMR-2004897, and by the UCLA PSEIF. Work at the ALS was supported by the Office of Science, Office of Basic Energy Sciences, of the US Department of Energy under contract number DE-AC02-05CH11231. The authors acknowledge the use of instruments at the Electron Imaging Center for NanoMachines supported by NIH 1S10RR23057 and the CNSI at UCLA. The authors also thank M. Murnane and J. Miao for encouragement and assistance in arranging the experiments.

References

[1] S. Behyan, B. Haines, C. Karanukaran, J. Wang, M. Obst, T. Tyliszczak, S. G. Urquhart, Surface Detection in a STXM Microscope, AIP Conference Proceedings 1365 (1) (2011) 184–187. doi:10.1063/1.3625335.

[2] J. Vila-Comamala, K. Jefimovs, J. Raabe, T. Pilvi, R. H. Fink, M. Senoner, A. Maaßdorf, M. Ritala, C. David, Advanced thin film technology for ultrahigh resolution X-ray microscopy, Ultramicroscopy 109 (11) (2009) 1360–1364. doi:10.1016/j.ultramic.2009.07.005.
URL http://www.sciencedirect.com/science/article/pii/S0304399109001661

[3] M. Obst, G. Schmid, 3d chemical mapping: application of scanning transmission (soft) X-ray microscopy (STXM) in combination with angle-scan tomography in bio-, geo-, and environmental sciences, Methods in Molecular Biology (Clifton, N.J.) 1117 (2014) 757–781. doi:10.1007/978-1-62703-776-1_34.

[4] E. G. Rightor, A. P. Hitchcock, H. Ade, R. D. Leapman, S. G. Urquhart, A. P. Smith, G. Mitchell, D. Fischer, H. J. Shin, T. Warwick, Spectromicroscopy of Poly(ethylene terephthalate): Comparison of Spectra and Radiation Damage Rates in X-ray Absorption and Electron Energy Loss, The Journal of Physical Chemistry B 101 (11) (1997) 1950–1960, publisher: American Chemical Society. doi:10.1021/jp9622748.
URL https://doi.org/10.1021/jp9622748

[5] A. F. G. Leontowich, A. P. Hitchcock, R. F. Egerton, Radiation damage yields across the carbon 1s excitation edge, Journal of Electron Spectroscopy and Related Phenomena 206 (2016) 58–64. doi:10.1016/j.elspec.2015.11.010.
URL http://www.sciencedirect.com/science/article/pii/S0368204815002844

[6] J. Kirz, C. Jacobsen, M. Howells, Soft X-ray microscopes and their biological applications, Quarterly Reviews of Biophysics 28 (1) (1995) 33–130. doi:10.1017/S0033583500003139.
URL https://www.cambridge.org/core/journals/quarterly-reviews-of-biophysics/article/soft-xray-microscopes-and-their-biological-applications/23BB8B16B05396A85B4773993620222A

[7] K. Shinohara, T. Ohigashi, S. Toné, M. Kado, A. Ito, Quantitative analysis of mammalian chromosome by scanning transmission soft X-ray microscopy, Ultramicroscopy 194 (2018) 1–6. doi:10.1016/j.ultramic.2018.07.001.
URL http://www.sciencedirect.com/science/article/pii/S0304399117304126

[8] K. Litzius, I. Lemesh, B. Krüger, P. Bassirian, L. Caretta, K. Richter, F. Büttner, K. Sato, O. A. Tretiakov, J. Förster, R. M. Reeve, M. Weigand, I. Bykova, H. Stoll, G. Schütz, G. S. D. Beach, M. Kläui, Skyrmion Hall effect revealed by direct time-resolved X-ray microscopy, Nature Physics 13 (2) (2017) 170–175, number: 2 Publisher: Nature Publishing Group. doi:10.1038/nphys4000.
URL https://www.nature.com/articles/nphys4000

[9] X. Ye, J. E. Schmidt, R.-P. Wang, I. K. v. Ravenhorst, R. Oord, T. Chen, F. d. Groot, F. Meirer, B. M. Weckhuysen, Deactivation of Cu-Exchanged Automotive-Emission NH3-SCR Catalysts Elucidated with Nanoscale Resolution Using Scanning Transmission X-ray Microscopy, Angewandte Chemie 132 (36) (2020) 15740–15747, _eprint: https://onlinelibrary.wiley.com/doi/pdf/10.1002/ange.201916554. doi:https://doi.org/10.1002/ange.201916554.

URL https://onlinelibrary.wiley.com/doi/abs/10.1002/ange.201916554

[10] W. Li, Z. Wang, F. Zhao, M. Li, X. Gao, Y. Zhao, J. Wang, J. Zhou, Y. Hu, Q. Xiao, X. Cui, M. J. Eslamibidgoli, M. H. Eikerling, R. Li, F. Brandys, R. Divigalpitiya, T.-K. Sham, X. Sun, Phosphorene Degradation: Visualization and Quantification of Nanoscale Phase Evolution by Scanning Transmission X-ray Microscopy, Chemistry of Materials 32 (3) (2020) 1272–1280, publisher: American Chemical Society. doi:10.1021/acs.chemmater.9b04811.
URL https://doi.org/10.1021/acs.chemmater.9b04811

[11] O. F. Vyvenko, T. Buonassisi, A. A. Istratov, H. Hieslmair, A. C. Thompson, R. Schindler, E. R. Weber, X-ray beam induced current—a synchrotron radiation based technique for the in situ analysis of recombination properties and chemical nature of metal clusters in silicon, Journal of Applied Physics 91 (6) (2002) 3614–3617. doi:10.1063/1.1450026.
URL https://aip.scitation.org/doi/10.1063/1.1450026

[12] B. Watts, D. Queen, A. L. D. Kilcoyne, T. Tyliszczak, F. Hellman, H. Ade, Soft X-ray beam induced current technique, Journal of Physics: Conference Series 186 (2009) 012023. doi:10.1088/1742-6596/186/1/012023.
URL http://stacks.iop.org/1742-6596/186/i=1/a=012023?key=crossref.fbb9c0bc6b46433b2dbf69bf2007e655

[13] D. P. Bernstein, B. Bräuer, R. Kukreja, J. Stöhr, T. Hauet, J. Cucchiara, S. Mangin, J. A. Katine, T. Tyliszczak, K. W. Chou, Y. Acremann, Nonuniform switching of the perpendicular magnetization in a spin-torque-driven magnetic nanopillar, Physical Review B 83 (18) (2011) 180410. doi:10.1103/PhysRevB.83.180410.
URL https://link.aps.org/doi/10.1103/PhysRevB.83.180410

[14] A. Koehl, H. Wasmund, A. Herpers, P. Guttmann, S. Werner, K. Henzler, H. Du, J. Mayer, R. Waser, R. Dittmann, Evidence for multifilamentary valence changes in resistive switching SrTiO3 devices detected by transmission X-ray microscopy, APL Materials 1 (4) (2013) 042102. doi:10.1063/1.4822438.
URL https://aip.scitation.org/doi/10.1063/1.4822438

[15] J. Lim, Y. Li, D. H. Alsem, H. So, S. C. Lee, P. Bai, D. A. Cogswell, X. Liu, N. Jin, Y.-s. Yu, N. J. Salmon, D. A. Shapiro, M. Z. Bazant, T. Tyliszczak, W. C. Chueh, Origin and hysteresis of lithium compositional spatiodynamics within battery primary particles, Science 353 (6299) (2016) 566–571. doi:10.1126/science.aaf4914.
URL https://science.sciencemag.org/content/353/6299/566

[16] A. Erbil, G. S. Cargill III, R. Frahm, R. F. Boehme, Total-electron-yield current measurements for near-surface extended x-ray-absorption fine structure, Physical Review B 37 (5) (1988) 2450–2464. doi:10.1103/PhysRevB.37.2450.
URL https://link.aps.org/doi/10.1103/PhysRevB.37.2450

[17] G. B. Kim, H. J. Song, H. J. Shin, C. K. Hong, X-ray absorption spectroscopy in total electron yield mode of scanning photoelectron microscopy, Journal of Electron Spectroscopy and Related Phenomena 148 (3) (2005) 137–141. doi:10.1016/j.elspec.2005.04.005.

[18] B. H. Frazer, B. Gilbert, B. R. Sonderegger, G. De Stasio, The probing depth of total electron yield in the sub-keV range: TEY-XAS and X-PEEM, Surface Science 537 (1-3) (2003) 161–167. doi:10.1016/S0039-6028(03)00613-7.
URL http://linkinghub.elsevier.com/retrieve/pii/S0039602803006137

[19] M. Stuckelberger, B. West, T. Nietzold, B. Lai, J. M. Maser, V. Rose, M. I. Bertoni, Engineering solar cells based on correlative X-ray microscopy, Journal of Materials Research 32 (10) (2017) 1825–1854. doi:10.1557/jmr.2017.108.
URL https://www.cambridge.org/core/product/identifier/S088429141700108X/type/journal_article

[20] L. Chayanun, V. Dagytė, A. Troian, D. Salomon, M. Borgström, J. Wallentin, Spectrally resolved x-ray beam induced current in a single InGaP nanowire, Nanotechnology 29 (45) (2018) 454001. doi:10.1088/1361-6528/aadc76.

[21] T. E. Everhart, O. C. Wells, R. K. Matta, A novel method of semiconductor device measurements, Proceedings of the IEEE 52 (12) (1964) 1642–1647. doi:10.1109/PROC.1964.3460.

[22] H. J. Leamy, Charge collection scanning electron microscopy, Journal of Applied Physics 53 (6) (1982) R51–R80. doi:10.1063/1.331667.
URL http://aip.scitation.org/doi/abs/10.1063/1.331667

[23] W. A. Hubbard, M. Mecklenburg, H. L. Chan, B. C. Regan, STEM Imaging with Beam-Induced Hole and Secondary Electron Currents, Physical Review Applied 10 (4) (2018) 044066. doi:10.1103/PhysRevApplied.10.044066.
URL https://link.aps.org/doi/10.1103/PhysRevApplied.10.044066

[24] M. Mecklenburg, W. A. Hubbard, J. J. Lodico, B. C. Regan, Electron beam-induced current imaging with two-angstrom resolution, Ultramicroscopy 207 (2019) 112852. doi:10.1016/j.ultramic.2019.112852.
URL http://www.sciencedirect.com/science/article/pii/S0304399119302311

[25] W. A. Hubbard, Z. Lingley, J. Theiss, S. Sitzman, T. Ayvazian, M. Brodie, B. Foran, Scanning transmission electron microscope mapping of electronic transport in polycrystalline BaTiO $_3$ ceramic capacitors, Applied Physics Letters 115 (13) (2019) 133502. doi:10.1063/1.5117055.
URL http://aip.scitation.org/doi/10.1063/1.5117055

[26] J. Maser, C. Jacobsen, J. Kirz, A. Osanna, S. Spector, S. Wang, J. Warnking, Development of a Cryo Scanning Transmission X-Ray Microscope at the NSLS, in: J. Thieme, G. Schmahl, D. Rudolph, E. Umbach (Eds.), X-Ray Microscopy and Spectromicroscopy: Status Report from the Fifth International Conference, Würzburg, August 19–23, 1996, Springer, Berlin, Heidelberg, 1998, pp. 35–44. doi:10.1007/978-3-642-72106-9_4.
URL https://doi.org/10.1007/978-3-642-72106-9_4

[27] D. A. Shapiro, R. Celestre, B. Enders, J. Joseph, H. Krishnan, M. A. Marcus, K. Nowrouzi, H. Pad-

593 more, J. Park, A. Warwick, Y.-S. Yu, The COSMIC
594 Imaging Beamline at the Advanced Light Source: a
595 new facility for spectro-microscopy of nano-materials,
596 Microscopy and Microanalysis 24 (S2) (2018) 8–11.
597 doi:10.1017/S1431927618012485.
598 [28] P. Denes, D. Doering, H. A. Padmore, J.-P. Walder,
599 J. Weizeorick, A fast, direct x-ray detection charge-
600 coupled device, Review of Scientific Instruments 80 (8)
601 (2009) 083302. doi:10.1063/1.3187222.
602 URL http://aip.scitation.org/doi/10.1063/1.
603 3187222
604 [29] S. Marchesini, H. Krishnan, B. J. Daurer, D. A.
605 Shapiro, T. Perciano, J. A. Sethian, F. R. N. C. Maia,
606 SHARP: a distributed GPU-based ptychographic
607 solver, Journal of Applied Crystallography 49 (4) (2016)
608 1245–1252, number: 4 Publisher: International Union
609 of Crystallography. doi:10.1107/S1600576716008074.
610 URL http://scripts.iucr.org/cgi-bin/paper?
611 jo5020